PIER C

(Received 9 March 2026, Accepted 16 April 2026, Scheduled 29 April 2026)

Variable Reaching Law Nonsingular Fast Terminal Sliding Mode Observer-Based Deadbeat Fault-tolerant Compensation Control for IPMSM's Demagnetization Fault

Dingdou Wen[1], Dengliang Xia[1], Xiaorui Wei[2], Wenjie Wu[1], and Yuanyuan Xiao[3,*]

[1]*Hunan University of Technology, Zhuzhou 412007, China*
[2]*Hunan University, Changsha 410082, China*
[3]*Hunan Open University, Changsha 410004, China*

ABSTRACT: To address the issues of electromagnetic torque attenuation and insufficient robustness caused by demagnetization faults in interior permanent magnet synchronous motors (IPMSMs), a deadbeat fault-tolerant compensation control (DBFTCC) strategy based on a variable reaching law nonsingular fast terminal sliding mode observer (VRL-NFTSMO) is proposed. First, the VRL-NFTSMO is designed to achieve a precise observation of the flux linkage and next current value. Second, DBFTCC is constructed based on flux linkage and current information, which can effectively suppress electromagnetic torque attenuation caused by demagnetization faults, improve system robustness, and achieve reliable fault-tolerant control under demagnetization faults. Finally, the experimental results indicate that the proposed compensation strategy has stronger fault tolerance and robustness than traditional methods when the IPMSMs suffer from both demagnetization fault and large load variation.

1. INTRODUCTION

Currently, interior permanent magnet synchronous motors (IPMSMs) are widely applied in fields such as rail transit, deep-sea exploration, high-end medical treatment, and wind power generation owing to their simple structure, high power density, and excellent operational stability [1–4].

To ensure the stable operation of the IPMSMs, various advanced control strategies have been proposed in academia and industry, such as fuzzy proportional integral (PI) control [5], sliding mode control (SMC) [6], model predictive control (MPC) [7], and deadbeat predictive current control (DPCC) [8, 9]. Excellent current control performance is the key to improving the dynamic and static quality of control systems [10]. Compared with other control strategies, DPCC demonstrates stronger control performance in current control scenarios owing to its faster current response speed and higher tracking accuracy.

However, IPMSMs typically operate in complex environments, such as high temperatures, strong electromagnetic interference, and harmonic pollution. Permanent magnets (PMs) are prone to demagnetization faults, leading to a significant deterioration of motor control performance and electromagnetic torque attenuation [11]. The main methods for diagnosing demagnetization faults include the nonlinear transformation method [12], back-EMF method [13], and observer method [14, 15]. To achieve effective detection of PM demagnetization, although a traditional sliding-mode observer (SMO) can observe the flux linkage, the observed values are not sufficiently precise. In [16], the fast Fourier transform is used to analyze the stator current signal of a permanent magnet synchronous motor, achieving the detection of demagnetization faults; however, it is difficult to apply to dynamic working conditions. In [17], the demagnetization fault of a permanent magnet synchronous motor is diagnosed based on the harmonic characteristics of the back-electromotive force; however, the anti-interference ability is weak and the diagnosis is prone to failure. In [18], an adaptive forgetting factor, recursive least squares flux linkage observer was constructed to observe flux linkage values; however, it is sensitive to disturbances and complex to adjust the parameters. In [19], a method based on current analysis is proposed to obtain disturbances caused by flux linkage mismatch, which can calculate the actual flux linkage value of the motor; however, it has a low separation accuracy.

In [16–19], the diagnosis of demagnetization fault is achieved; however, no effective solution is proposed for fault-tolerant control after the fault. After the motor demagnetization fault, the d-q axis flux linkage value changes. Owing to the reliance of the traditional DPCC on model accuracy, it leads to inaccurate DPCC prediction and reduced system stability. To achieve continuous and stable operation after the IPMSM's demagnetization fault, a new control method is proposed in [20], which improves the robustness of the system by constructing an improved ultra-local model and using SMO to estimate the unknown terms in the model. In [21], an equivalent input disturbance fault-tolerant control method based on improved SMO is proposed, which decouples speed and state errors by the observer and improves the system's anti-interference ability. In [22], the integral terminal SMO is

* Corresponding author: Yuanyuan Xiao (494492524@qq.com).

adopted to consider demagnetization fault during modeling, eliminating the weight factor parameter tuning steps and obtaining the optimal control law to achieve fault-tolerant control. In [23], a robust fault-tolerant predictive current control algorithm based on a composite observer is designed, which observes the predicted value of compensation voltage and current in real time, and adds a compensation voltage regulation link to improve the robustness of the system. In [24], a fault-tolerant method combining fuzzy extended state observer and sliding mode control is proposed to detect and reconstruct demagnetization fault, thereby enhancing the anti-interference ability of the motor. However, in [20–24], fault-tolerant control strategies have not been able to solve the problem of electromagnetic torque attenuation caused by demagnetization fault. When a demagnetization fault and a sudden large load change occur, the motor cannot maintain normal operation without real-time torque compensation.

In summary, to address the issues of electromagnetic torque attenuation and insufficient robustness caused by demagnetization faults in IPMSMs, a deadbeat fault-tolerant compensation control (DBFTCC) strategy based on a variable reaching law nonsingular fast terminal sliding mode observer (VRL-NFTSMO) is proposed. Compared with the SMOs and NFTSMOs reported in [20–23], the proposed VRL-NFTSMO integrates an improved nonsingular fast terminal sliding mode surface and a variable reaching law in its design. Torque compensation is achieved by combining VRL-NFTSMO with DBFTCC, improving the robustness of the system. The main contributions of this study are as follows:

(1) A VRL-NFTSMO is constructed, which can quickly and accurately observe the d-q axis flux linkage parameters.

(2) Based on the actual flux linkage observed by VRL-NFTSMO, a DBFTCC strategy is designed to output the optimal d-axis reference current during demagnetization faults, restoring the q-axis current to normal values and effectively compensating for the loss of torque.

The remainder of this article is structured as follows. In Section 2, the mathematical model of the IPMSMs for normal operation and demagnetization fault is established. In Section 3, the DPCC method for normal and demagnetization fault conditions is constructed. In Section 4, the implementation mechanism of the DBFTCC strategy is explored. In Section 5, the design principle of VRL-NFTSMO is described. In Section 6, the experimental results and analysis are presented. Finally, the conclusions are presented.

2. MATHEMATICAL MODEL OF NORMAL AND DEMAGNETIZATION FOR IPMSMS

2.1. Normal Mathematical Model of IPMSMs

The normal voltage equation for the IPMSMs in d-q coordinate system can be expressed as [25]:

$$\begin{cases} u_d = \frac{d\varphi_d}{dt} - \omega_e \varphi_q + R i_d \\ u_q = \frac{d\varphi_q}{dt} + \omega_e \varphi_d + R i_q \end{cases} \tag{1}$$

The stator flux linkage equation is expressed as follows:

$$\begin{cases} \varphi_d = \varphi_{ro} + L_d i_d \\ \varphi_q = L_q i_q \end{cases} \tag{2}$$

where u_d, u_q, i_d, and i_q denote the d-q axis stator voltages and stator currents, respectively. R, ω_e, L_d, and L_q denote the stator resistance, electrical angular velocity, d-axis stator inductance, and q-axis stator inductance, respectively. φ_d and φ_q are the stator flux of d-q axis respectively. φ_{ro} is the PM flux linkage.

The electromagnetic torque equation is expressed as follows:

$$T_e = 1.5 n_p \left[\left(L_d - L_q \right) i_d i_q + \varphi_{ro} i_q \right] \tag{3}$$

where T_e is the electromagnetic torque, and n_p is the number of pole pairs.

The effective flux linkage of the IPMSMs is defined as [26]:

$$\varphi_{act} = \left(L_d - L_q \right) i_d + \varphi_{ro} \tag{4}$$

2.2. The Demagnetization Mathematical Model of IPMSMs

When demagnetization occurs in IPMSMs, the amplitude of the PM flux linkage changes from φ_{ro} to φ_r, and its magnetic declination angle λ changes from 0° to (0°, 90°). The flux linkage relationship is shown in Fig. 1. (2) is rewritten as

$$\begin{cases} \varphi_d = \varphi_{ro} + L_d i_d + \Delta\varphi_{rd} = L_d i_d + \varphi_{rd} \\ \varphi_q = L_q i_q + \Delta\varphi_{rq} = L_q i_q + \varphi_{rq} \end{cases} \tag{5}$$

$$\begin{cases} \varphi_{rd} = \varphi_{ro} + \Delta\varphi_{rd} = \varphi_r \cos\lambda \\ \varphi_{rq} = \Delta\varphi_{rq} = \varphi_r \sin\lambda \end{cases} \tag{6}$$

where φ_{rd} and φ_{rq} are the d-q axis flux linkage components, respectively; $\Delta\varphi_{rd}$ and $\Delta\varphi_{rq}$ are the variations in d-q axis flux linkage, respectively.

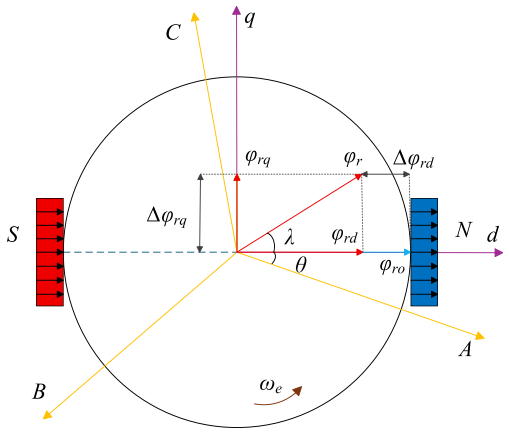

FIGURE 1. Relationship diagram of PM flux linkage.

Substituting (5) and (6) into (1), the demagnetization voltage equation of the IPMSMs can be expressed as:

$$\begin{cases} u_d = L_d \frac{di_d}{dt} + R i_d - \omega_e L_q i_q - \omega_e \varphi_{rq} \\ u_q = L_q \frac{di_q}{dt} + R i_q + \omega_e L_d i_d + \omega_e \varphi_{rd} \end{cases} \tag{7}$$

The demagnetization electromagnetic torque equation of IPMSMs is expressed as:

$$T_e = 1.5 n_p \left[\left(L_d - L_q \right) i_d i_q + \varphi_{rd} i_q - \varphi_{rq} i_d \right] \tag{8}$$

3. DPCC CONTROL PRINCIPLE

3.1. The DPCC Control Principle for Normal Operation

Performing first-order Eulerian discretization on (1), the DPCC predictive voltage for normal operation of IPMSMs is:

$$\begin{cases} u_d^*(k) = L_d \frac{i_d^*(k+1) - i_d(k)}{T_s} + Ri_d(k) - L_q \omega_e(k) i_q(k) \\ u_q^*(k) = L_q \frac{i_q^*(k+1) - i_q(k)}{T_s} + Ri_q(k) + L_d \omega_e(k) i_d(k) \\ \qquad + \omega_e(k) \varphi_{ro} \end{cases} \tag{9}$$

where u_d^*, u_q^*, i_d^*, and i_q^* denote the d-q axis reference voltages and currents, respectively.

3.2. The DPCC Control Principle for Demagnetization Fault

By performing first-order Eulerian discretization in (7), the DPCC predictive voltage for the demagnetization fault of the IPMSMs is expressed as follows:

$$\begin{cases} u_d^*(k) = L_d \frac{i_d^*(k+1) - i_d(k)}{T_s} + Ri_d(k) \\ \qquad - L_q \omega_e(k) i_q(k) - \omega_e(k) \varphi_{rq} \\ u_q^*(k) = L_q \frac{i_q^*(k+1) - i_q(k)}{T_s} + Ri_q(k) \\ \qquad + L_d \omega_e(k) i_d(k) + \omega_e(k) \varphi_{rd} \end{cases} \tag{10}$$

4. DESIGN OF DBFTCC METHOD

From (3), for DPCC control with $i_d = 0$, the effective flux is inversely proportional to i_q at the same electromagnetic torque. When the IPMSMs suffer a demagnetization fault, i_q increases abruptly. However, the output capacity of the inverter is limited, and i_q reaches its limit. i_d can only be adjusted by DBFTCC to compensate for the loss of torque and reduce i_q output.

From (4), the demagnetization fault effective flux linkage equation of the IPMSMs is expressed as:

$$\varphi_{act} = (L_d - L_q) i_d + \varphi_{rd} \tag{11}$$

Performing first-order Euler discretization on (7), the d-axis current equation is:

$$L_d [i_d(k+1) - i_d(k)] = T_s \omega_e(k) L_q i_q(k) + T_s u_d(k) - T_s R i_d(k) + T_s \omega_e(k) \varphi_{rq} \tag{12}$$

To obtain the d-axis reference current $i_d^{ref}(k+1)$, the d-axis current at time $k+1$ in (12) was considered as the reference current. (12) was rewritten as:

$$L_d \left[i_d^{ref}(k+1) - i_d(k) \right] = T_s \omega_e(k) L_q i_q(k) + T_s u_d(k) - T_s R i_d(k) + T_s \omega_e(k) \varphi_{rq} \tag{13}$$

To introduce the effective flux linkage, (13) is rewritten as:

$$\varphi_{act}(k+1) = T_s \omega_e(k) L_q i_q(k) + T_s u_d(k) - T_s R i_d(k) + T_s \omega_e(k) \varphi_{rq} + L_d i_d(k) + \varphi_{rd} + (L_d - L_q) i_d(k+1) - L_d i_d^{ref}(k+1) \tag{14}$$

where $\varphi_{act}(k+1) = \varphi_{rd} + (L_d - L_q) i_d(k+1)$. $\varphi_{act}(k+1)$ and $i_d(k+1)$ are obtained using the VRL-NFTSMO.

If the motor operates without a demagnetization fault at time k, a demagnetization fault occurs at time $k+1$. From (8), the torque exhibits a term $-\varphi_{rq} i_d$. It is unreasonable to make the effective flux linkage at time $k+1$ equal to that at time k. Owing to the presence of the error term $-\varphi_{rq} i_d$, the compensated electromagnetic torque is greater than that of the normal torque. As $i_d^{ref}(k+1)$ is larger than its ideal value, the stator current approaches its limit value. Owing to the limited output capacity of the inverter, the stator current cannot exceed this limit value. To enhance the fault-tolerant capability of the system, the effective flux linkage at time $k+1$ is equated to an effective flux linkage ϕ_{act} that enables compensation for the nominal electromagnetic torque, and a new d-axis reference current is obtained. (14) is rewritten as

$$\phi_{act} = T_s \omega_e(k) L_q i_q(k) + T_s u_d(k) - T_s R i_d(k) + T_s \omega_e(k) \varphi_{rq} + L_d i_d(k) + \varphi_{rd} + (L_d - L_q) i_d(k+1) - L_d i_d^{ref}(k+1) \tag{15}$$

To obtain a suitable effective flux linkage ϕ_{act}, based on the principle of deadbeat control, the electromagnetic torques before and after the demagnetization fault are equated, with the effective flux linkage post-fault replaced by ϕ_{act}, that is,

$$1.5 n_p \varphi_{ro} i_q(k) = 1.5 n_p [(L_d - L_q) i_d(k+1) i_q(k+1) + \varphi_{rd} i_q(k+1) - \varphi_{rq} i_d(k+1)] = 1.5 n_p [\phi_{act} i_q(k+1) - \varphi_{rq} i_d(k+1)] \tag{16}$$

(16) can be simplified as follows:

$$\phi_{act} = \frac{\varphi_{rq} i_d(k+1) + \varphi_{ro} i_q(k)}{i_q(k+1)} \tag{17}$$

To restore i_q to its normal value, let $i_q(k+1) = i_q(k)$, and (17) is rewritten as:

$$\phi_{act} = \frac{\varphi_{rq} i_d(k+1)}{i_q(k+1)} + \varphi_{ro} \tag{18}$$

Substituting (18) into (15), the flux linkage and current at time $k+1$ is replaced by the observed values. The expression is as follows:

$$i_d^{ref}(k+1) = \frac{1}{L_d} [T_s \omega_e(k) L_q i_q(k) + T_s u_d(k) - T_s R i_d(k) + T_s \omega_e(k) \hat{\varphi}_{rq} + L_d i_d(k)] + \frac{1}{L_d} \left[\hat{\varphi}_{rd} + (L_d - L_q) \hat{i}_d(k+1) - \varphi_{ro} - \frac{\hat{\varphi}_{rq} \hat{i}_d(k+1)}{\hat{i}_q(k+1)} \right] \tag{19}$$

When the IPMSMs operate normally, $\hat{\varphi}_{rd} + (L_d - L_q) \hat{i}_d(k+1) = \phi_{act} = \varphi_{ro}$ and $\varphi_{rq} = 0$, then $i_d^{ref}(k+1) = 0$. Therefore, the motor has no electromagnetic torque loss and does not require compensation. When a demagnetization fault occurs,

$\hat{\varphi}_{rd} + (L_d - L_q)\hat{i}_d(k+1) = \phi_{act} \neq \varphi_{ro}$ and $\varphi_{rq} \neq 0$. At this point, the output $i_d^{ref}(k+1)$ can compensate for the electromagnetic torque loss. In addition, owing to the limited output capacity of the inverter, $i_d^{ref}(k+1)$ must satisfy the following constraints:

$$i_d^{ref}(k+1) > -\sqrt{i_{\max}^2(k+1) - i_q^2(k+1)} \tag{20}$$

By substituting the flux linkage observation values into (10), the predicted voltage of the DPCC is as follows:

$$\begin{cases} u_d^*(k) = L_d \frac{i_d^*(k+1) - i_d(k)}{T_s} + Ri_d(k) \\ \qquad -L_q\omega_e(k) i_q(k) - \omega_e(k)\hat{\varphi}_{rq} \\ u_q^*(k) = L_q \frac{i_q^*(k+1) - i_q(k)}{T_s} + Ri_q(k) \\ \qquad +L_d\omega_e(k) i_d(k) + \omega_e(k)\hat{\varphi}_{rd} \end{cases} \tag{21}$$

Owing to the delay in the output $u*(k)$ of the inverter at time $k+1$ in traditional DPCC, the control voltage is delayed by one beat. To minimize the impact of the delay on the system control performance, let $i(k) = \hat{i}(k+1)$ and $i_d^*(k+1) = i_d^{ref}(k+1)$, then the expected voltage of the DBFTCC is as follows:

$$\begin{cases} u_d^*(k) = L_d \frac{i_d^{ref}(k+1) - \hat{i}_d(k+1)}{T_s} + Ri_d(k) \\ \qquad -L_q\omega_e(k) i_q(k) - \omega_e(k)\hat{\varphi}_{rq} \\ u_q^*(k) = L_q \frac{i_q^*(k+1) - \hat{i}_q(k+1)}{T_s} + Ri_q(k) \\ \qquad +L_d\omega_e(k) i_d(k) + \omega_e(k)\hat{\varphi}_{rd} \end{cases} \tag{22}$$

In addition, since $L_d = L_q$ in the surface permanent magnet synchronous motor (SPMSM), $(L_d - L_q)i_d = 0$. It is impossible for DBFTCC to compensate for the torque deficit by adjusting i_d. Therefore, the DBFTCC is not applicable to SPMSM.

5. DESIGN AND STABILITY ANALYSIS OF NONSINGULAR FAST TERMINAL SLIDING MODE OBSERVER BASED ON VARIABLE REACHING LAW

As shown in (19), to obtain $i_d^{ref}(k+1)$, the observed values of the flux linkage and current at time $k+1$ must be known. The designed VRL-NFTSMO algorithm can obtain accurate flux linkage and current parameters in this study.

(7) is rewritten as the state equation:

$$\begin{cases} \dot{\mathbf{x}} = \mathbf{Ax} + \mathbf{Bu} + \mathbf{Dd} \\ \mathbf{y} = \mathbf{Cx} \end{cases} \tag{23}$$

where $\mathbf{x} = [i_d\ i_q]^T$, $\mathbf{u} = [u_d\ u_q]^T$, $\mathbf{y} = [i_d\ i_q]^T$, $\mathbf{d} = [\varphi_{rd}\ \varphi_{rq}]^T$, **A**, **B**, **C**, and **D** is the coefficient matrix, where $\mathbf{A} = \begin{bmatrix} -\frac{R}{L_d} & \omega_e\frac{L_q}{L_d} \\ -\omega_e\frac{L_d}{L_q} & -\frac{R}{L_q} \end{bmatrix}$, $\mathbf{B} = \begin{bmatrix} \frac{1}{L_d} & 0 \\ 0 & \frac{1}{L_q} \end{bmatrix}$, $\mathbf{C} = \begin{bmatrix} 1 & 0 \\ 0 & 1 \end{bmatrix}$, $\mathbf{D} = \begin{bmatrix} 0 & \frac{\omega_e}{L_d} \\ -\frac{\omega_e}{L_q} & 0 \end{bmatrix}$.

The VRL-NFTSMO designed based on (23) is as follows:

$$\dot{\hat{\mathbf{x}}} = \mathbf{A}\hat{\mathbf{x}} + \mathbf{Bu} + \mathbf{v} \tag{24}$$

where $\hat{\mathbf{x}}$ is the observed value of $\mathbf{x}$, $\hat{\mathbf{x}} = \begin{bmatrix} \hat{i}_d\ \hat{i}_q \end{bmatrix}^T$. $\mathbf{v} = [v_d\ v_q]^T$ is the sliding mode term.

Subtracting (24) from (23) yields the error state equation:

$$\dot{\mathbf{e}} = \mathbf{Ae} + \mathbf{Dd} - \mathbf{v} \tag{25}$$

where $\mathbf{e}$ is the observation error, $\mathbf{e} = \mathbf{x} - \hat{\mathbf{x}}$.

To accelerate the convergence speed of the current error, the nonsingular fast terminal sliding surface is designed as follows:

$$\mathbf{s} = \boldsymbol{\alpha}\mathbf{e} + \boldsymbol{\beta}\dot{\mathbf{e}} + \boldsymbol{\eta}\mathbf{e}^{\frac{h}{r}} + \boldsymbol{\xi}\dot{\mathbf{e}}^{\frac{p}{q}} \tag{26}$$

where $\boldsymbol{\alpha}$, $\boldsymbol{\beta}$, $\boldsymbol{\eta}$, and $\boldsymbol{\xi}$ are the positive parameter matrices to be designed; h, r, p, and q are odd constants to be designed, such that $1 < h/r < 2$, $1 < p/q < 2$.

Taking the derivative of (26), the following expression is obtained:

$$\dot{\mathbf{s}} = \boldsymbol{\alpha}\dot{\mathbf{e}} + \boldsymbol{\beta}\ddot{\mathbf{e}} + \boldsymbol{\eta}\frac{h}{r}\mathbf{e}^{\frac{h}{r}-1}\dot{\mathbf{e}} + \boldsymbol{\xi}\frac{p}{q}\dot{\mathbf{e}}^{\frac{p}{q}-1}\ddot{\mathbf{e}} \tag{27}$$

To accelerate the convergence speed of SMO, an improved variable reaching law is expressed as follows:

$$\begin{aligned} \dot{\mathbf{s}} &= -\mathbf{k}_1|\mathbf{s}|^n \operatorname{sgn}(\mathbf{s}) - \mathbf{k}_2|\mathbf{s}|^m \operatorname{sgn}(\mathbf{s}) - \mathbf{k}_3\mathbf{s} \\ n &= \begin{cases} \mu & |\mathbf{s}| \geq 1 \\ \max\{1, |\mathbf{s}|\} & |\mathbf{s}| < 1 \end{cases} \end{aligned} \tag{28}$$

where $\mathbf{k}_1 = [k_{1d}\ k_{1q}]^T$, $\mathbf{k}_2 = [k_{2d}\ k_{2q}]^T$, $\mathbf{k}_3 = [k_{3d}\ k_{3q}]^T$, $n \geq 1$, $0 < m < 1$, $\mathbf{k}_1$, $\mathbf{k}_2$, $\mathbf{k}_3$ are positive parameter matrices to be designed, and n, m are positive parameters to be designed.

Owing to the introduction of the variable exponential design in the improved reaching law, when the system state satisfies $|\mathbf{s}| \geq 1$, the reaching law can be expressed as $\dot{\mathbf{s}} = -\mathbf{k}_1|\mathbf{s}|^{\mu}\operatorname{sgn}(\mathbf{s}) - \mathbf{k}_2|\mathbf{s}|^m\operatorname{sgn}(\mathbf{s}) - \mathbf{k}_3\mathbf{s}$. Its effect is equivalent to that of the novel double-power reaching law, which shortens the convergence time and accelerates the reaching speed. When the system state condition is $|\mathbf{s}| < 1$, the double-exponent power reaching law can be expressed as $\dot{\mathbf{s}} = -\mathbf{k}_1|\mathbf{s}| - \mathbf{k}_2|\mathbf{s}|^m\operatorname{sgn}(\mathbf{s}) - \mathbf{k}_3\mathbf{s}$, which is equivalent to the single-power fast reaching law. At this point, the system can smoothly enter the sliding surface and converge to the vicinity of the equilibrium point. This reaching law can effectively alleviate chattering, while the piecewise design guarantees global convergence.

Theorem 1: For the error state (25), if the sliding surface (26) and improved reaching law (28) are selected, the designed VRL-NFTSMO control law is as follows:

$$\begin{cases} \mathbf{v} = \mathbf{v}_{ed} + \mathbf{v}_o \\ \mathbf{v}_{ed} = \mathbf{Ae} \\ \mathbf{v}_o = \int_0^t \left[\begin{array}{l} \mathbf{k}_1|\mathbf{s}|^n \operatorname{sgn}(\mathbf{s}) + \mathbf{k}_2|\mathbf{s}|^m \operatorname{sgn}(\mathbf{s}) + \mathbf{k}_3\mathbf{s} \\ + \left(\boldsymbol{\alpha}\dot{\mathbf{e}} + \boldsymbol{\eta}\frac{h}{r}\mathbf{e}^{\frac{h}{r}-1}\dot{\mathbf{e}}\right)\left(\boldsymbol{\beta} + \boldsymbol{\xi}\frac{p}{q}\dot{\mathbf{e}}^{\frac{p}{q}-1}\right) \end{array} \right] d\tau \end{cases} \tag{29}$$

where the VRL-NFTSMO control law comprises $\mathbf{v}_o$ and $\mathbf{v}_{ed}$. $\mathbf{v}_o$ is a switching control law that allows the state variable to quickly reach the sliding surface $\mathbf{s}$, whereas $\mathbf{v}_{ed}$ is an equivalent control law that ensures that the state variable remains at $\mathbf{s} = 0$ after reaching $\mathbf{s}$.

Proof 1: The selected Lyapunov function V is as follows:

$$V = \frac{1}{2}\mathbf{s}^2 \tag{30}$$

Taking the derivative of (30) and substituting (28) yields:

$$\begin{aligned}\dot{V} &= \mathbf{s}\dot{\mathbf{s}} \\ &= \mathbf{s}\left[-\mathbf{k}_1 |\mathbf{s}|^n \operatorname{sgn}(\mathbf{s}) - \mathbf{k}_2 |\mathbf{s}|^m \operatorname{sgn}(\mathbf{s}) - \mathbf{k}_3\mathbf{s}\right] \\ &= -\mathbf{k}_1 |\mathbf{s}|^{n+1} \operatorname{sgn}(\mathbf{s}) - \mathbf{k}_2 |\mathbf{s}|^{m+1} \operatorname{sgn}(\mathbf{s}) - \mathbf{k}_3\mathbf{s}^2 \\ &\leq 0\end{aligned} \tag{31}$$

if and only if $\mathbf{s} = 0$, $\mathbf{s}\dot{\mathbf{s}} = 0$.

According to the continuity of the system, the existence theorem and reachability definition of the sliding mode reaching law, if $\mathbf{s}\dot{\mathbf{s}} \leqslant 0$ is satisfied, the designed reaching law satisfies the sliding mode reachability condition, and the double power exponential law designed using (28) can converge to the equilibrium point.

Theorem 2: For the improved double-power exponential variable reaching law of (28), assuming that the initial state of $\mathbf{s}$ is $\mathbf{s}_0$, the corresponding states $\mathbf{s}$ and $\dot{\mathbf{s}}$ both reach the sliding surface and converge to 0 within a finite time, with a convergence time less than $(\mathbf{t}_1 + \mathbf{t}_2 + \mathbf{t}_3)$. Here, t_1, t_2 and t_3 are the time for $\mathbf{s}_0$ to $\mathbf{s}(t_1)$, $\mathbf{s}(t_1)$ to $\mathbf{s}(t_2)$, and $\mathbf{s}(t_2)$ to $\mathbf{s}(t_3)$, respectively.

Taking $|\mathbf{s}| \geq 1$ as an example, the convergence time $\mathbf{t}_1$, $\mathbf{t}_2$ and $\mathbf{t}_3$ are respectively:

$$\begin{aligned}\mathbf{t}_1 = \frac{1}{(1-\mu)\mathbf{k}_3}\Bigg[&\ln\left(\mathbf{s}_0^{1-\mu} + \frac{\mathbf{k}_1}{\mathbf{k}_3}\operatorname{sgn}(\mathbf{s}_0)\right) \\ &- \ln\left(\mu^{1-\mu} + \frac{\mathbf{k}_1}{\mathbf{k}_3}\operatorname{sgn}(\mathbf{s}_0)\right)\Bigg]\end{aligned} \tag{32}$$

$$\begin{aligned}\mathbf{t}_2 = \frac{1}{(m-1)\mathbf{k}_3}\Bigg[&\ln\left(m^{1-m} + \frac{\mathbf{k}_2}{\mathbf{k}_3}\operatorname{sgn}(\mathbf{s}_0)\right) \\ &- \ln\left(1 + \frac{\mathbf{k}_2}{\mathbf{k}_3}\operatorname{sgn}(\mathbf{s}_0)\right)\Bigg]\end{aligned} \tag{33}$$

$$\begin{aligned}\mathbf{t}_3 = \frac{1}{(m-1)(\mathbf{k}_1+\mathbf{k}_3)}\Bigg[&\ln\left(m^{1-m} + \frac{\mathbf{k}_2}{\mathbf{k}_1+\mathbf{k}_3}\operatorname{sgn}(\mathbf{s}_0)\right) \\ &- \ln\left(1 + \frac{\mathbf{k}_2}{\mathbf{k}_1+\mathbf{k}_3}\operatorname{sgn}(\mathbf{s}_0)\right)\Bigg]\end{aligned} \tag{34}$$

Proof 2: Taking $1 < \mu < \mathbf{s}_0$ as an example, the global process is divided into three stages.

In the first stage, the system reaches from $\mathbf{s}_0$ to $\mathbf{s}_{t1}$, and (28) can be rewritten as:

$$\dot{\mathbf{s}} = -\mathbf{k}_1\mathbf{s}^{\mu} - \mathbf{k}_2\mathbf{s}^{m} - \mathbf{k}_3\mathbf{s} \tag{35}$$

To solve (35), because of the excessive number of unknown parameters, the equation can be solved in two steps. Firstly, the process of solving the equation $\dot{\mathbf{s}} + \mathbf{k}_1\mathbf{s}^{\mu} = -\mathbf{k}_3\mathbf{s}$ is as follows:

$$\mathbf{s}^{-\mu}\frac{d\mathbf{s}}{dt} + \mathbf{k}_3\mathbf{s}^{1-\mu} = -\mathbf{k}_1 \tag{36}$$

Assuming the existence of an intermediate variable $\mathbf{y} = \mathbf{s}^{1-\mu}$, (36) can be expressed as:

$$-(1-\mu)\mathbf{k}_1 = \frac{d\mathbf{y}}{dt} + (1-\mu)\mathbf{k}_3\mathbf{y} \tag{37}$$

Let $\mathbf{y} = \mathbf{u}(t)\exp(-\int(1-\mu)\mathbf{k}_3 dt)$, where $\mathbf{u} = \mathbf{u}(t)$ is a continuous function. Substituting into (37) yields:

$$\frac{d\mathbf{u}}{dt} = -(1-\mu)\mathbf{k}_1 \exp\left(\int (1-\mu)\mathbf{k}_3 dt\right) \tag{38}$$

Integrating (38) yields:

$$\mathbf{u} = \int -(1-\mu)\mathbf{k}_1 \exp\left(\int (1-\mu)\mathbf{k}_3 dt\right) dt + \mathbf{C} \tag{39}$$

where $\mathbf{C}$ is a constant.

$$\begin{aligned}\mathbf{y} = &\left[\int -(1-\mu)\mathbf{k}_1 \exp\left(\int (1-\mu)\mathbf{k}_3 dt\right) dt + \mathbf{C}\right] \\ &\exp\left(-\int (1-\mu)\mathbf{k}_3 dt\right) = \mathbf{C}\exp\left(-\int (1-\mu)\mathbf{k}_3 dt\right) \\ &- \left[\frac{\mathbf{k}_1}{\mathbf{k}_3}\exp\left(\int (1-\mu)\mathbf{k}_3 dt\right)\right]\exp\left(-\int (1-\mu)\mathbf{k}_3 dt\right) \\ = &\ \mathbf{C}\exp\left(-\int (1-\mu)\mathbf{k}_3 dt\right) - \frac{\mathbf{k}_1}{\mathbf{k}_3}\end{aligned} \tag{40}$$

Simplifying (40) yields:

$$\mathbf{s}^{1-\mu} = \mathbf{C}\exp\left(-\int (1-\mu)\mathbf{k}_3 dt\right) - \frac{\mathbf{k}_1}{\mathbf{k}_3} \tag{41}$$

Setting time $t = 0$, the constant $\mathbf{C}$ can be solved as:

$$\mathbf{C} = \mathbf{s}_0^{1-\mu} + \frac{\mathbf{k}_1}{\mathbf{k}_3} \tag{42}$$

From (41) and (42), $\mathbf{t}_1$ can be obtained:

$$\mathbf{t}_1 = \frac{1}{(1-\mu)\mathbf{k}_3}\left[\ln\left(\mathbf{s}_0^{1-\mu} + \frac{\mathbf{k}_1}{\mathbf{k}_3}\right) - \ln\left(\mu^{1-\mu} + \frac{\mathbf{k}_1}{\mathbf{k}_3}\right)\right] \tag{43}$$

Similarly, $\mathbf{t}_2$ and $\mathbf{t}_3$ can be obtained as follows:

$$\mathbf{t}_2 = \frac{1}{(m-1)\mathbf{k}_3}\left[\ln\left(m^{1-m} + \frac{\mathbf{k}_2}{\mathbf{k}_3}\right) - \ln\left(1 + \frac{\mathbf{k}_2}{\mathbf{k}_3}\right)\right] \tag{44}$$

$$\mathbf{t}_3 = \frac{1}{(m-1)(\mathbf{k}_1+\mathbf{k}_3)}\left[\ln\left(m^{1-m} + \frac{\mathbf{k}_2}{\mathbf{k}_1+\mathbf{k}_3}\operatorname{sgn}(\mathbf{s}_0)\right)\right.$$

TABLE 1. The parameters of IPMSMs.

Parameters	Values
Direct current voltage (U_{dc})	1500 V
Rotational inertia (J)	1 kg·m^2
Viscous friction coefficient (B)	0.001 Nm·s/rad
Stator resistance (R)	0.02 Ω
d-axis inductance (L_d)	0.0015 H
q-axis inductance (L_q)	0.003572 H
PM flux linkage (φ_{ro})	0.892 Wb
Polar logarithm (n_p)	4

$$-\ln\left(1+\frac{\mathbf{k}_2}{\mathbf{k}_1+\mathbf{k}_3}c\left(\mathbf{s}_0\right)\right)\Bigg] \tag{45}$$

Therefore, the time required for the system to move from $\mathbf{s}(t_1)=1$ to $\mathbf{s}(t_2)=m$ and from $\mathbf{s}(t_2)=m$ to $\mathbf{s}(t_3)=0$ is less than $\mathbf{t}_2$ and $\mathbf{t}_3$, respectively, indicating that the total convergence time required by the system is less than $(\mathbf{t}_1+\mathbf{t}_2+\mathbf{t}_3)$.

Taking the derivative of (30) and substituting (27) yields:

$$\begin{aligned}\dot{V} &= \mathbf{s}\dot{\mathbf{s}}\\ &= \mathbf{s}\left[\boldsymbol{\alpha}\dot{\mathbf{e}}+\boldsymbol{\eta}\frac{h}{r}\mathbf{e}^{\frac{h}{r}-1}\dot{\mathbf{e}}+\left(\boldsymbol{\beta}+\boldsymbol{\xi}\frac{p}{q}\dot{\mathbf{e}}^{\frac{p}{q}-1}\right)\ddot{\mathbf{e}}\right]\\ &= \mathbf{s}\left(\boldsymbol{\beta}+\boldsymbol{\xi}\frac{p}{q}\dot{\mathbf{e}}^{\frac{p}{q}-1}\right)\left(\ddot{\mathbf{e}}+\frac{\boldsymbol{\alpha}\dot{\mathbf{e}}+\boldsymbol{\eta}\frac{h}{r}\mathbf{e}^{\frac{h}{r}-1}\dot{\mathbf{e}}}{\boldsymbol{\beta}+\boldsymbol{\xi}\frac{p}{q}\dot{\mathbf{e}}^{\frac{p}{q}-1}}\right)\end{aligned} \tag{46}$$

Taking the derivative of (25) and substituting (46) yields:

$$\dot{V}=\mathbf{s}\left(\boldsymbol{\beta}+\boldsymbol{\xi}\frac{p}{q}\dot{\mathbf{e}}^{\frac{p}{q}-1}\right)\left(\mathbf{A}\dot{\mathbf{e}}+\mathbf{D}\dot{\mathbf{d}}-\dot{\mathbf{v}}+\frac{\boldsymbol{\alpha}\dot{\mathbf{e}}+\boldsymbol{\eta}\frac{h}{r}\mathbf{e}^{\frac{h}{r}-1}\dot{\mathbf{e}}}{\boldsymbol{\beta}+\boldsymbol{\xi}\frac{p}{q}\dot{\mathbf{e}}^{\frac{p}{q}-1}}\right) \tag{47}$$

Taking the derivative of (29) and substituting (47) yields:

$$\begin{aligned}\dot{V} &= -\left(\boldsymbol{\beta}+\boldsymbol{\xi}\frac{p}{q}\dot{\mathbf{e}}^{\frac{p}{q}-1}\right)\left(\mathbf{k}_1|\mathbf{s}|^{n+1}+\mathbf{k}_3|\mathbf{s}|^2\right.\\ &\quad\left.+|\mathbf{s}|\left(\mathbf{k}_2|\mathbf{s}|^m-\mathbf{D}\dot{\mathbf{d}}\right)\right)\end{aligned} \tag{48}$$

(48) can also be rewritten as:

$$\begin{aligned}\dot{V} &= -\left(\boldsymbol{\beta}+\boldsymbol{\xi}\frac{p}{q}\dot{\mathbf{e}}^{\frac{p}{q}-1}\right)\left(\mathbf{k}_2|\mathbf{s}|^{m+1}+\mathbf{k}_3|\mathbf{s}|^2\right.\\ &\quad\left.+|\mathbf{s}|\left(\mathbf{k}_1|\mathbf{s}|^n-\mathbf{D}\dot{\mathbf{d}}\right)\right)\end{aligned} \tag{49}$$

Assuming that $\mathbf{k}_2|\mathbf{s}|^m-\mathbf{D}\dot{\mathbf{d}}\geqslant 0$, $\mathbf{k}_1|\mathbf{s}|^n-\mathbf{D}\dot{\mathbf{d}}\geqslant 0$, $\mathbf{k}_1>0$, $\mathbf{k}_2>0$, $\mathbf{k}_3>0$, $p/q>0$, and $\dot{\mathbf{e}}^{p/q-1}>0$, then $|\mathbf{D}\dot{\mathbf{d}}|$ is bounded.

From (48), it can be inferred that:

$$\dot{V}\leq-\left(\boldsymbol{\beta}+\boldsymbol{\xi}\frac{p}{q}\dot{\mathbf{e}}^{\frac{p}{q}-1}\right)\left(\mathbf{k}_1|\mathbf{s}|^{n+1}+\mathbf{k}_3|\mathbf{s}|^2\right)\leq 0 \tag{50}$$

From (49), it can be inferred that:

$$\dot{V}\leq-\left(\boldsymbol{\beta}+\boldsymbol{\xi}\frac{p}{q}\dot{\mathbf{e}}^{\frac{p}{q}-1}\right)\left(\mathbf{k}_2|\mathbf{s}|^{m+1}+\mathbf{k}_3|\mathbf{s}|^2\right)\leq 0 \tag{51}$$

TABLE 2. The parameters of the sliding mode observer.

SMO	VRL-NFTSMO
$k_d=50000$	$\alpha=200$
$k_q=50000$	$\beta=4$
\	$\eta=200$
\	$\xi=0.01$
\	$\mu=1.8$
\	$m=0.8$
\	$k_1=5000$
\	$k_2=5000$
\	$k_3=9500$
\	$h/r=5/3$
\	$p/q=7/5$

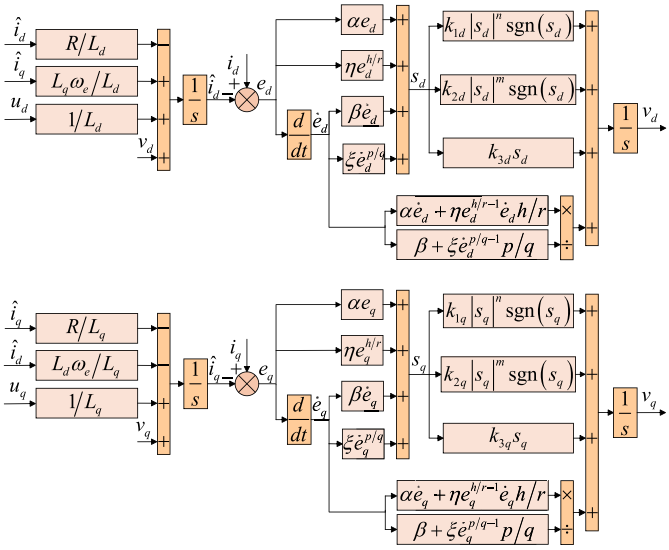

FIGURE 2. The block diagram of VRL-NFTSMO.

From (50) and (51), it can be seen that due to $\dot{V}\leqslant 0$, the state variable will reach the sliding surface in a finite time.

According to (24), the predicted current value observed by VRL-NFTSMO at the next moment is expressed as follows:

$$\begin{cases}\hat{i}_d(k+1)=\hat{i}_d(k)-\frac{T_sR}{L_d}\hat{i}_d(k)+\frac{T_s}{L_d}u_d(k)\\ \qquad\qquad+\frac{T_sL_q\omega_e(k)}{L_d}\hat{i}_q(k)+\frac{T_s\omega_e(k)}{L_d}\hat{\varphi}_{rq}\\ \hat{i}_q(k+1)=\hat{i}_q(k)-\frac{T_sR}{L_q}\hat{i}_q(k)+\frac{T_s}{L_q}u_q(k)\\ \qquad\qquad-\frac{T_sL_d\omega_e(k)}{L_q}\hat{i}_d(k)-\frac{T_s\omega_e(k)}{L_q}\hat{\varphi}_{rd}\end{cases} \tag{52}$$

The block diagram of the VRL-NFTSMO is shown in Fig. 2, and the system block diagram of DBFTCC based on the VRL-NFTSMO is shown in Fig. 3.

6. EXPERIMENTAL RESULTS AND ANALYSIS

Because the demagnetization fault is difficult to simulate in real motors, a hardware in the loop simulation experiment (HILS) platform was established based on RT-LAB to verify the feasibility and effectiveness of the proposed algorithm, as shown

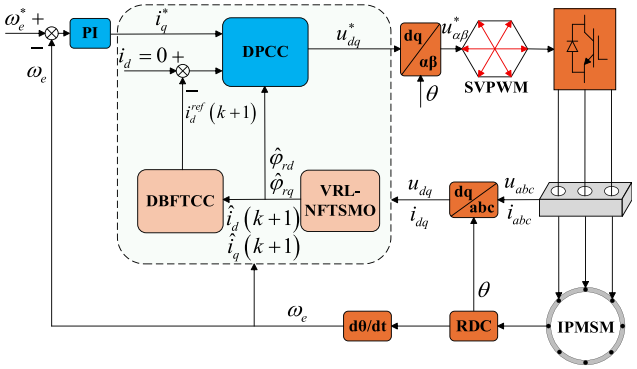

FIGURE 3. The system block diagram of DBFTCC based on VRL-NFTSMO.

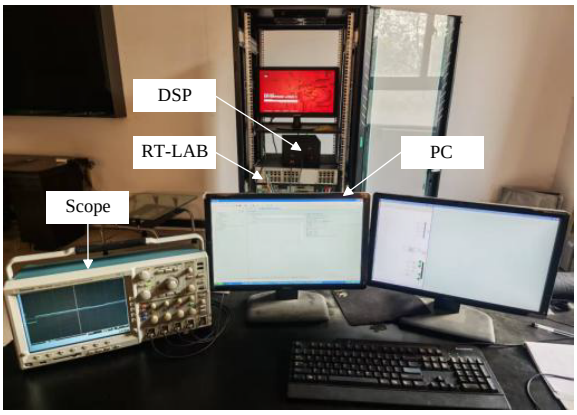

FIGURE 4. RT-LAB experimental platform.

in Fig. 4. The DSP adopts TMS320F2812, and the demagnetization fault of the IPMSMs was simulated using RT-LAB (OP5600).

The IPMSMs' control strategy adopts $i_d = 0$. The parameters of the IPMSMs are listed in Table 1, and the parameters of the sliding mode observer are listed in Table 2. The experimental results of the DPCC, DBFTCC-SMO, and DBFTCC-VRL-NFTSMO methods were compared to verify the superiority of the proposed method.

Remark 1: k_d, k_q ($k_d > 0$, $k_q > 0$) are the exponential convergence law parameters in SMO. First, select a sufficiently large value to make the system converge, and then perform fine tuning.

Remark 2: The selection of sliding mode surface parameters in VRL-NFTSMO directly affects the stability of the motor control system. After selecting the approximate parameters of α, β, η, ξ, h/r and p/q to confirm system stability, fine tuning is performed, α, β, η, ξ, h/r and p/q become larger, causing the system to overshoot during transients. α, β, η, ξ, h/r and p/q become smaller, causing a slower speed response and a longer time to reach the given value. k_1, k_2, and k_3 are the convergence law parameters, and the control law is to improve the dynamic quality of the convergence motion of the sliding mode variable structure. Within the specified range of the parameters, after several simulations to select the approximate appropriate k_1, k_2 and k_3, and then fine tuning to obtain better control effect. μ and m are used to optimize the jitter problem of the sliding mode motion.

Experimental conditions: The motor starts with no load, and the reference speed ω_e^* is 300 r/min. At $t = 0.2$ s, the load torque T_L increases from 0 to 650 N·m. At $t = 0.65$ s, the IPMSMs are demagnetized; the flux amplitude of PM decreases from $\varphi_{ro} = 0.892$ Wb to 0.6 Wb; and the magnetic deflection angle λ changes from 0 to $\pi/6$ rad. At 1.1 s, T_L decreases to 550 N·m. At 1.55 s, T_L increases to 750 N·m. The total running time is 2 s.

Figures 5, 6, 7, and 8 show the speed, electromagnetic torque, d-axis, and q-axis current waveforms of the DPCC, DBFTCC-SMO, and DBFTCC-VRL-NFTSMO methods, respectively. Figs. 9, 10, and 11 show the d-axis reference current, d-axis, and q-axis flux linkage observation waveforms of DBFTCC-SMO and DBFTCC-VRL-NFTSMO, respectively.

(1) Result analysis without demagnetization fault

Before 0.65 s, as shown in Figs. 5–8, the speeds of DPCC, DBFTCC-SMO, and DBFTCC-VRL-NFTSMO strategies are maintained at 300 r/min, and the electromagnetic torque T_e output is 650 N·m, with i_d and i_q stable at 0 A and 122 A, respectively. Therefore, the speed, electromagnetic torque, and d-q axis current output of the three methods are normal, indicating that the IPMSMs are in normal operation.

As shown in Fig. 9, the output of $i_d^{ref}(k+1)$ for both DBFTCC-SMO and DBFTCC-VRL-NFTSMO is 0 A, which is consistent with the theoretical value.

As shown in Figs. 10 and 11, the observed values φ_{rd} of SMO and VRL-NFTSMO are stabilized at 0.8918 Wb and 0.892 Wb, respectively, and φ_{rq} are stabilized at 0 Wb and 0 Wb, respectively, whereas the theoretical values of φ_{rd} and φ_{rq} are 0.892 Wb and 0 Wb, respectively. Therefore, VRL-NFTSMO can observe the flux linkage more accurately during normal operation, and its flux linkage observation accuracy is better than that of SMO, reducing the motor's ripples of ω_e and T_e, minimizing the impact of inaccurate flux observation on fault-tolerant control, and further improving the robustness of the system. Compared with DPCC, DBFTCC adopts the observed flux linkage by the observer instead of the nominal flux linkage, and the motor speed, electromagnetic torque, d-q axis currents, and output of $i_d^{ref}(k+1)$ are consistent, which does not affect the normal operation of the motor.

(2) Result analysis with demagnetization fault

At 0.65 s, the PM was demagnetized.

As shown in Figs. 5–8, with the DPCC method, when T_L was 650 N·m, T_e only output 620 N·m, which is lower than T_L, resulting in a significant drop in speed and i_q quickly reaching the limit value of 200 A. At 1.1 s, when T_L decreased to 550 N·m, T_e could not output 550 N·m in time. At 1.55 s, when T_L increased to 750 N·m, T_e only output 620 N·m, and the speed decreased rapidly. In contrast, with the DBFTCC-SMO and DBFTCC-VRL-NFTSMO methods, the demagnetization fault occurred at 0.65 s, and T_L decreased to 550 N·m and increased to 750 N·m at 1.1 s and 1.55 s, respectively. The speed was maintained at 300 r/min, 300 r/min, and 300 r/min, respectively, and T_e output 650 N·m, 550 N·m, and 750 N·m, respectively,

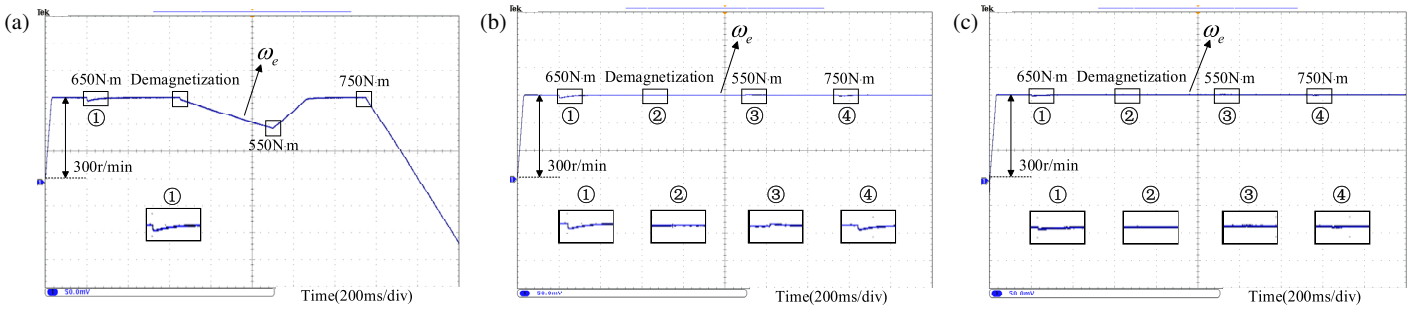

FIGURE 5. The waveform of the speed. (a) DPCC. (b) DBFTCC-SMO. (c) DBFTCC-VRL-NFTSMO.

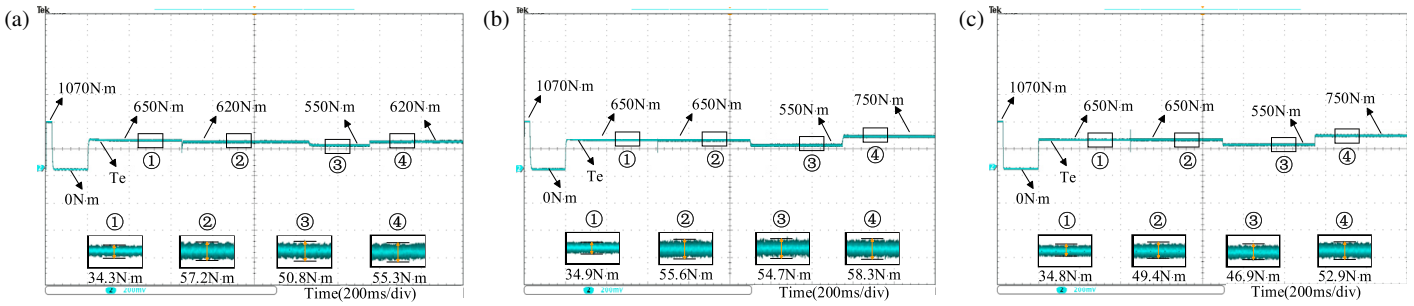

FIGURE 6. The waveform of the electromagnetic torque. (a) DPCC. (b) DBFTCC-SMO. (c) DBFTCC-VRL-NFTSMO.

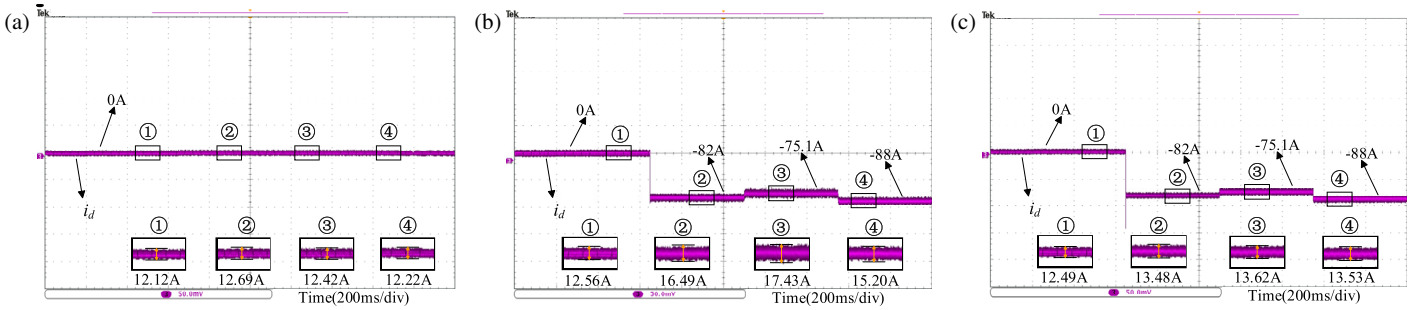

FIGURE 7. The waveform of the d-axis current. (a) DPCC. (b) DBFTCC-SMO. (c) DBFTCC-VRL-NFTSMO.

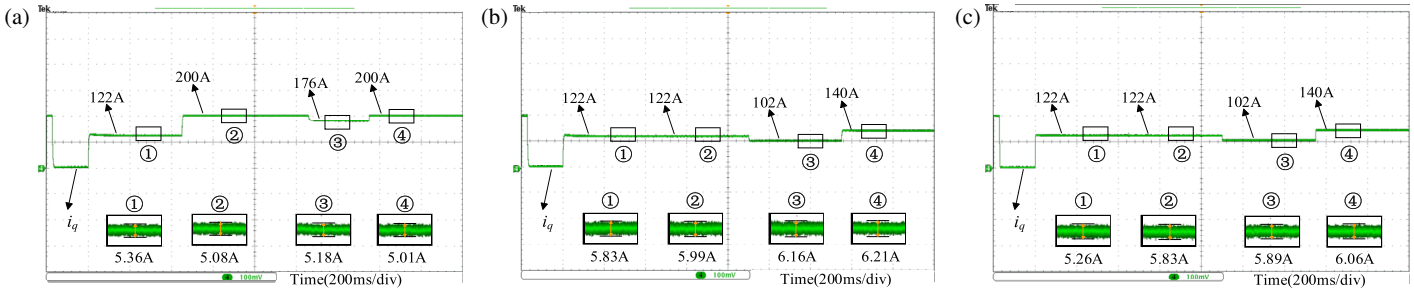

FIGURE 8. The waveform of the q-axis current. (a) DPCC. (b) DBFTCC-SMO. (c) DBFTCC-VRL-NFTSMO.

which are consistent with T_L. Compared with DBFTCC-SMO, DBFTCC-VRL-NFTSMO had a smaller torque ripple, and i_q did not suddenly increase to the limit value, stabilizing at 122 A, 102 A, and 140 A, respectively. Therefore, when the load suddenly changed significantly, the proposed DBFTCC method can compensate for the lack of T_e during demagnetization, maintain normal speed, and improve the robustness of the system.

As shown in Fig. 9, the proposed DBFTCC method can output data in a timely manner to compensate for the missing torque after an IPMSMs demagnetization fault. When T_L was 650 N·m, 550 N·m, and 750 N·m, the theoretical calculated values of $i_d^{ref}(k+1)$ were -82.1 A, -74.8 A, and -88.2 A, re-

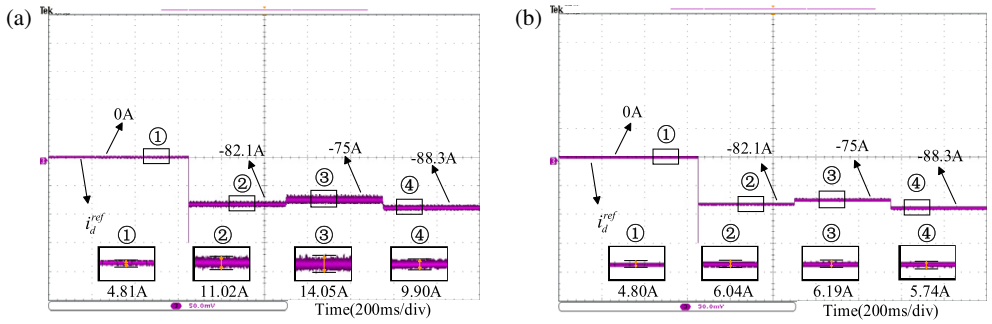

FIGURE 9. The waveform of the d-axis reference current. (a) DBFTCC-SMO. (b) DBFTCC-VRL-NFTSMO.

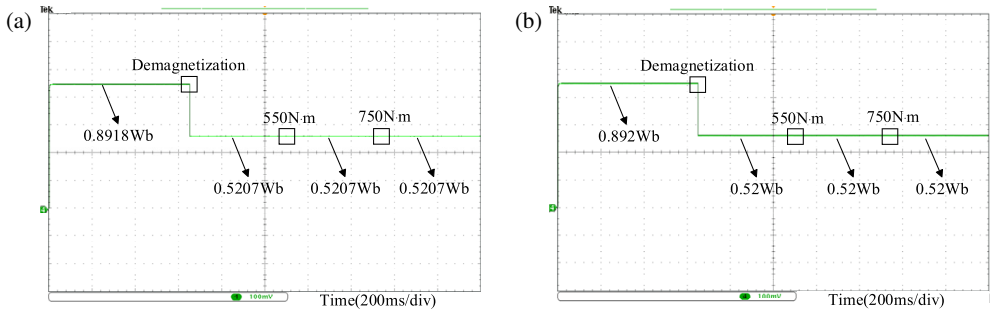

FIGURE 10. The waveform of the d-axis flux linkage. (a) DBFTCC-SMO. (b) DBFTCC-VRL-NFTSMO.

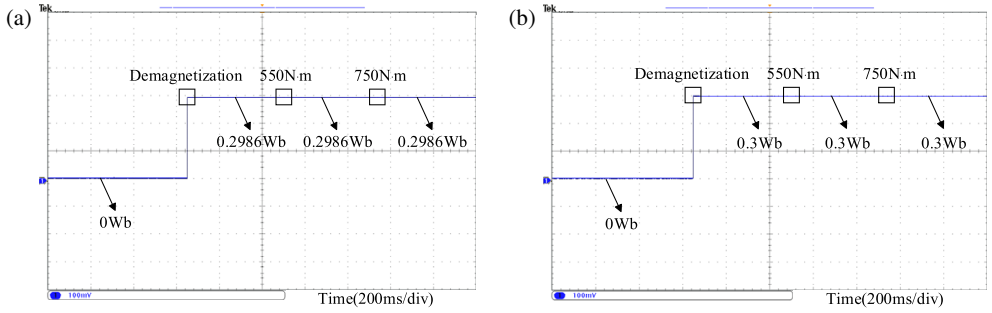

FIGURE 11. The waveform of the q-axis flux linkage. (a) DBFTCC-SMO. (b) DBFTCC-VRL-NFTSMO.

TABLE 3. Comprehensive performance comparison of IPMSMs demagnetization control strategies.

Parameter	Method	Value (%)
ω_e	DBFTCC-SMO	0.0011/0.0055/0.0108
	DBFTCC-VRL-NFTSMO	0.0009/0.0019/0.0038
T_e	DBFTCC-SMO	0.0855/0.0995/0.0777
	DBFTCC-VRL-NFTSMO	0.0760/0.0853/0.0705
i_d^{ref}	DBFTCC-SMO	0.0923/0.1072/0.0834
	DBFTCC-VRL-NFTSMO	0.0736/0.0824/0.0652

spectively, and the constraint values were -158.5 A, -172.1 A, and -142.8 A, respectively. Within the constraint range, the $i_d^{ref}(k+1)$ output values of DBFTCC-SMO and DBFTCC-VRL-NFTSMO were consistent with the theoretical ones.

As shown in Figs. 10 and 11, after the demagnetization fault at 0.65 s, T_L decreased to 550 N·m and increased to 750 N·m at 1.1 s and 1.55 s, respectively. The observed values φ_{rd} of SMO and VRL-NFTSMO stabilized at 0.5207 Wb and 0.52 Wb, respectively, and φ_{rq} stabilized at 0.2986 Wb and 0.3 Wb, respectively, whereas the theoretical values of φ_{rd} and φ_{rq} were 0.5196 Wb and 0.3 Wb, respectively. The results demonstrated that VRL-NFTSMO could more accurately observe the flux linkage during demagnetization faults and large-load sudden coupling, with a higher flux observation accuracy than SMO. In combination with DBFTCC, the ripples of ω_e, T_e, and i_d^{ref} were reduced, and the influence of the impact flux parameter on fault-tolerant control was minimized, further improving the robustness of the system.

A comprehensive performance comparison of the IPMSMs demagnetization control strategies is presented in Table 3, and the performance comparison of the flux-linkage observer is presented in Table 4.

TABLE 4. Performance comparison of flux linkage observers.

Parameter	Observer	Observed value	MAPE (%)
φ_{rq}	SMO	0/0.2986/0.2986/0.2986	0/0.47/0.47/0.47
	VRL-NFTSMO	0/0.3/0.3/0.3	0/0/0/0
φ_{rd}	SMO	0.8918/0.5207/0.5207/0.5207	0.02/0.21/0.21/0.21
	VRL-NFTSMO	0.892/0.52/0.52/0.52	0/0.08/0.08/0.08

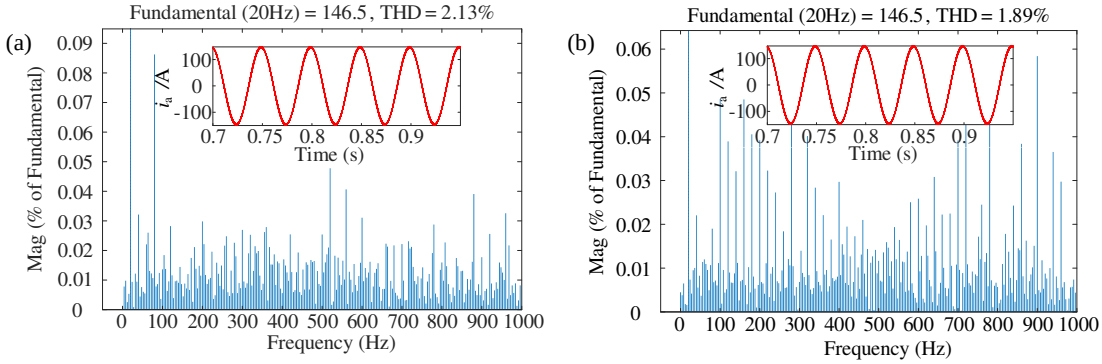

FIGURE 12. The THD analysis of phase-A stator current. (a) DBFTCC-SMO. (b) DBFTCC-VRL-NFTSMO.

Remark 3: 1/2/3 denote three operating conditions: 1. Demagnetization fault of the IPMSMs. 2. IPMSMs demagnetization fault and load drop. 3. IPMSMs demagnetization fault and load increase.

Remark 4: 1/2/3/4 denote four operating conditions: 1. IPMSMs without demagnetization. 2. IPMSMs demagnetization. 3. IPMSMs demagnetization and load drop. 4. IPMSMs demagnetization and load increase.

(3) THD analysis with demagnetization fault

The total harmonic distortion (THD value of the phase-A stator current during demagnetization is shown in Fig. 12. As shown in Fig. 12, the THD values of DBFTCC-SMO and DBFTCC-VRL-NFTSMO were 2.13% and 1.89%, respectively. The VRL-NFTSMO enables more accurate observation of flux linkage values, leading to smoother current reference values and PWM voltage outputs. Finally, harmonic distortion in the system is significantly suppressed. These results indicate that DBFTCC-VRL-NFTSMO had a better effect on suppressing harmonics.

In summary, both DBFTCC-SMO and DBFTCC-VRL-NFTSMO can compensate for the torque loss caused by PM demagnetization, thereby improving the robustness of the system. When the IPMSMs demagnetize, the control effect of DBFTCC-VRL-NFTSMO is better than that of DBFTCC-SMO, and VRL-NFTSMO can more accurately observe the flux linkage, outputting more accurate magnetic flux observation values for DBFTCC, thus avoiding adverse effects on fault-tolerant control caused by inaccurate flux linkage observation.

7. CONCLUSION

In this study, a DBFTCC method based on VRL-NFTSMO is proposed, which can accurately observe the flux linkage, effectively compensate for torque loss caused by demagnetization faults, and suppress the degradation of control performance, further improving the system's fault tolerance and robustness. The main conclusions obtained from the experimental analysis are as follows:

(1) Compared with the DPCC method, the proposed DBFTCC can compensate for torque loss after demagnetization fault and quickly adjust the torque output, thereby improving the fault tolerance capability of the system.

(2) VRL-NFTSMO can observe the flux linkage more accurately, avoiding the degradation of fault tolerance caused by inaccurate flux observation. Additionally, the combination of VRL-NFTSMO and DBFTCC optimizes the output accuracy of $i_d^{ref}(k+1)$ and enhances the robustness of the motor.

(3) Compared with DBFTCC-SMO, when demagnetization and load sudden changes occur simultaneously, the proposed DBFTCC-VRL-NFTSMO method reduces speed ripple, torque ripple, and total harmonic distortion by 49.48%, 11.55%, and 11.27%, respectively, further improving the stability of the system.

This study focuses on the investigation of IPMSM's performance under demagnetization fault and sudden load change scenarios. The next step will explore the impact mechanism of motor parameter mismatch on control systems.

REFERENCES

[1] Wei, D., K. Liu, W. Hu, X. Peng, Y. Chen, and R. Ding, "Short-time adaline based fault feature extraction for inter-turn short circuit diagnosis of PMSM via residual insulation monitoring," *IEEE Transactions on Industrial Electronics*, Vol. 70, No. 3, 3103–3114, 2023.

[2] Perera, A. and R. Nilsen, "Recursive prediction error gradient-based algorithms and framework to identify PMSM parameters online," *IEEE Transactions on Industry Applications*, Vol. 59,

No. 2, 1788–1799, 2023.

[3] Toloue, S. F., S. H. Kamali, and M. Moallem, "Torque ripple minimization and control of a permanent magnet synchronous motor using multiobjective extremum seeking," *IEEE/ASME Transactions on Mechatronics*, Vol. 24, No. 5, 2151–2160, 2019.

[4] Nasiri, M., S. Mobayen, and A. Arzani, "PID-type terminal sliding mode control for permanent magnet synchronous generator-based enhanced wind energy conversion systems," *CSEE Journal of Power and Energy Systems*, Vol. 8, No. 4, 993–1003, 2022.

[5] Jung, J.-W., V. Q. Leu, T. D. Do, E.-K. Kim, and H. H. Choi, "Adaptive PID speed control design for permanent magnet synchronous motor drives," *IEEE Transactions on Power Electronics*, Vol. 30, No. 2, 900–908, 2015.

[6] Xu, B., L. Zhang, and W. Ji, "Improved non-singular fast terminal sliding mode control with disturbance observer for PMSM drives," *IEEE Transactions on Transportation Electrification*, Vol. 7, No. 4, 2753–2762, 2021.

[7] Zhang, X., Z. Liu, P. Zhang, and Y. Zhang, "Model predictive current control for PMSM drives based on nonparametric prediction model," *IEEE Transactions on Transportation Electrification*, Vol. 10, No. 1, 711–719, 2024.

[8] Li, X., S. Zhang, X. Cui, Y. Wang, C. Zhang, Z. Li, and Y. Zhou, "Novel deadbeat predictive current control for PMSM with parameter updating scheme," *IEEE Journal of Emerging and Selected Topics in Power Electronics*, Vol. 10, No. 2, 2065–2074, 2022.

[9] Xu, Y., S. Li, and J. Zou, "Integral sliding mode control based deadbeat predictive current control for PMSM drives with disturbance rejection," *IEEE Transactions on Power Electronics*, Vol. 37, No. 3, 2845–2856, 2022.

[10] Sun, Z., Y. Deng, J. Wang, T. Yang, Z. Wei, and H. Cao, "Finite control set model-free predictive current control of PMSM with two voltage vectors based on ultralocal model," *IEEE Transactions on Power Electronics*, Vol. 38, No. 1, 776–788, 2023.

[11] Faiz, J. and E. Mazaheri-Tehrani, "Demagnetization modeling and fault diagnosing techniques in permanent magnet machines under stationary and nonstationary conditions: An overview," *IEEE Transactions on Industry Applications*, Vol. 53, No. 3, 2772–2785, 2017.

[12] Song, X., J. Zhao, J. Song, F. Dong, L. Xu, and J. Zhao, "Local demagnetization fault recognition of permanent magnet synchronous linear motor based on S-transform and PSO-LSSVM," *IEEE Transactions on Power Electronics*, Vol. 35, No. 8, 7816–7825, 2020.

[13] Li, Z., S. Zhao, X. Yang, J. Cao, and J. Li, "Partial demagnetization fault diagnosis of interior permanent magnet synchronous motor based on back electromotive force constant of a new search coil," *IEEE Transactions on Instrumentation and Measurement*, Vol. 74, 1–12, 2025.

[14] Ye, S. and X. Yao, "A modified flux sliding-mode observer for the sensorless control of PMSMs with online stator resistance and inductance estimation," *IEEE Transactions on Power Electronics*, Vol. 35, No. 8, 8652–8662, 2020.

[15] Zhao, K.-H., T.-F. Chen, C.-F. Zhang, J. He, and G. Huang, "Online fault detection of permanent magnet demagnetization for ipmsms by nonsingular fast terminal-sliding-mode observer," *Sensors*, Vol. 14, No. 12, 23 119–23 136, 2014.

[16] Rosero, J. A., J. Cusido, A. Garcia, J. A. Ortega, and L. Romeral, "Study on the permanent magnet demagnetization fault in permanent magnet synchronous machines," in *IECON 2006 — 32nd Annual Conference on IEEE Industrial Electronics*, 879–884, Paris, France, 2006.

[17] Jin, P., Y. Yuan, Q. Xu, S. Fang, H. Lin, and S. L. Ho, "Analysis of axial-flux halbach permanent-magnet machine," *IEEE Transactions on Magnetics*, Vol. 51, No. 11, 1–4, 2015.

[18] Feng, W., M. Li, W. Zhang, S. Huang, and H. Zhang, "Sliding mode fault-tolerant control based on fast convergence law for faults of PMSM," *Chinese Journal of Electrical Engineering*, Vol. 10, No. 3, 147–157, 2024.

[19] Han, Y., S. Chen, C. Gong, X. Zhao, F. Zhang, and Y. Li, "Accurate SM disturbance observer-based demagnetization fault diagnosis with parameter mismatch impacts eliminated for IPM motors," *IEEE Transactions on Power Electronics*, Vol. 38, No. 5, 5706–5710, 2023.

[20] Zhao, K., T. Yin, C. Zhang, J. He, X. Li, Y. Chen, R. Zhou, and A. Leng, "Robust model-free nonsingular terminal sliding mode control for PMSM demagnetization fault," *IEEE Access*, Vol. 7, 15 737–15 748, 2019.

[21] Zhao, K., R. Zhou, J. She, C. Zhang, J. He, G. Huang, and X. Li, "Demagnetization-fault reconstruction and tolerant-control for PMSM using improved SMO-based equivalent-input-disturbance approach," *IEEE/ASME Transactions on Mechatronics*, Vol. 27, No. 2, 701–712, 2022.

[22] Hu, F., D. Luo, C. Luo, Z. Long, and G. Wu, "Cascaded robust fault-tolerant predictive control for PMSM drives," *Energies*, Vol. 11, No. 11, 3087, 2018.

[23] Zhang, C., G. Wu, F. Rong, J. Feng, L. Jia, J. He, and S. Huang, "Robust fault-tolerant predictive current control for permanent magnet synchronous motors considering demagnetization fault," *IEEE Transactions on Industrial Electronics*, Vol. 65, No. 7, 5324–5334, 2018.

[24] Zeghlache, A., H. Mekki, A. Djerioui, and M. F. Benkhoris, "Active fault-tolerant control for surface permanent magnet synchronous motor under demagnetization fault," *Periodica Polytechnica Electrical Engineering and Computer Science*, Vol. 68, No. 1, 12–20, 2023.

[25] Wang, H., C. Gan, C. Zhang, H. Ren, and R. Qu, "Parameter robust predictive current control for PMSM drives based on self-tuning incremental model and voltage constraint compensation," *IEEE Transactions on Power Electronics*, Vol. 40, No. 8, 11 268–11 282, 2025.

[26] Woldegiorgis, A. T., X. Ge, H. Wang, and Y. Zuo, "An active flux estimation in the estimated reference frame for sensorless control of IPMSM," *IEEE Transactions on Power Electronics*, Vol. 37, No. 8, 9047–9060, 2022.